AGU PUBLICATIONS

JGR

Journal of Geophysical Research: Oceans

RESEARCH ARTICLE

10.1002/2014JC010131

Key Points:
- Surface water diluted by heavy rain had low $pCO_{2,sw}$
- Passage of a tropical depression led to high $pCO_{2,sw}$ by eddy-driven uplifting
- The depression turned local water from a carbon sink to a source temporarily

Correspondence to:
D. L. Tang,
lingzistdl@126.com

Citation:
Sun, Q., D. L. Tang, L. Legendre, and P. Shi (2014), Enhanced sea-air CO_2 exchange influenced by a tropical depression in the South China Sea, *J. Geophys. Res. Oceans*, *119*, doi:10.1002/2014JC010131.

Received 8 MAY 2014
Accepted 11 SEP 2014
Accepted article online 18 SEP 2014

Enhanced sea-air CO_2 exchange influenced by a tropical depression in the South China Sea

Qingyang Sun[1,2], DanLing Tang[1,2], Louis Legendre[3,4], and Ping Shi[1,2]

[1]Research Center for Remote Sensing and Marine Ecology & Environment, State Key Laboratory of Tropical Oceanography, South China Sea Institute of Oceanology, Chinese Academy of Sciences, Guangzhou, China, [2]University of the Chinese Academy of Sciences, School of Ocean Sciences, Beijing, China, [3]Laboratoire d'Océanographie de Villefranche, UMR 7093, UPMC Université Paris 06, Sorbonne Universités, Villefranche-sur-Mer, France, [4]Laboratoire d'Océanographie de Villefranche, CNRS, UMR 7093, Villefranche-sur-Mer, France

Abstract Ship measurements made 2 days after the passage of a tropical depression (TD) in the South China Sea (SCS, April 2011) showed two contrasted responses of the partial pressure of CO_2 at sea surface ($pCO_{2,sw}$). In low sea-surface salinity (SSS) water, $pCO_{2,sw}$ was low (349 $\pm$ 7 μatm), and the area was a carbon sink (-4.7 ± 1.8 mmol CO_2 m^{-2} d^{-1}), whereas in water with high SSS and chlorophyll *a* and low dissolved oxygen and sea surface temperature, $pCO_{2,sw}$ was higher than for normal SCS water (376 $\pm$ 8 versus 362 $\pm$ 4 μatm) and the area was a carbon source (1.2 $\pm$ 3.1 mmol CO_2 m^{-2} d^{-1}). Satellite data showed two large areas of low SSS before the TD, which were likely influenced by rainfall, and these areas were considered to have low $pCO_{2,sw}$ because of their low SSS. The high $pCO_{2,sw}$ after the TD is explained by the uplifting to the surface of deeper and CO_2-rich water, due to winds accompanied by the TD. The difference in sea-air CO_2 flux between the TD-affected area and the lower-SSS water was 1.99 + 4.70 = 6.7 mmol CO_2 m^{-2} d^{-1}, indicating a 100% change caused by the TD compared to the average seasonal value in spring in southern SCS (3.3 $\pm$ 0.3 mmol CO_2 m^{-2} d^{-1}). Undersaturation of CO_2 prior to the TD due to dilution by freshwater and the preexisting cold eddy, and slow translation speed of the TD, are considered to account for the CO_2 flux change.

1. Introduction

Numerous observations and investigations conducted on weekly to interannual time scales have shown that the global ocean acts as a sink of anthropogenic carbon dioxide (CO_2) [*Takahashi et al*., 1993, 2002; *Bates*, 2007; *Wanninkhof et al*., 2007; *Zhai et al*., 2013]. The partial pressure of CO_2 in surface water of the ocean ($pCO_{2,sw}$), which is a crucial factor in sea-air exchange of CO_2 and transfer of carbon from surface to deep waters by the three ocean carbon pumps (solubility, carbonate, and soft-tissue or organic or biological [*Volk and Hoffert*, 1985]), seems to be sensitive to episodic events, such as tropical cyclones (also called typhoons, hurricanes, and storms), frontal and eddy-driven upwelling and mixing. Tropical cyclones have great influence on marine ecosystems, such as cooling of sea surface temperature (SST) [*Price*, 1981; *Bond et al*., 2011; *Zhao et al*., 2009], increased dissolved oxygen [*Lin et al*., 2014], enhanced phytoplankton blooms [*Zhao et al*., 2009; *Hung et al*., 2010; *Chung et al*., 2012; *Ye et al*., 2013], higher export of particulate organic carbon out of the euphotic zone [*Hung et al*., 2010; *Chen et al*., 2013; *Shih et al*., 2013], and increased phytoplankton biomass [*Chung et al*., 2012; *Tsuchiya et al*., 2014] and fish abundance [*Yu et al*., 2013, 2014]. An early study [*Bates et al*., 1998] found that cooling of SST resulting from tropical cyclone had great impact on $pCO_{2,sw}$ and other processes, e.g., upward mixing and entrainment of deep water rich in dissolved inorganic carbon (DIC, i.e., CO_2, HCO_3^-, and CO_3^{2-}). Similarly, the enhanced biological activity (e.g., respiration and photosynthesis) associated with tropical cyclone greatly influences $pCO_{2,sw}$ [*Borges and Frankignoulle*, 2001; *Perrie et al*., 2004; *Huang and Imberger*, 2010; *Bond et al*., 2011; *Mahadevan et al*., 2011; *Wada et al*., 2011]. The presence of cold (cyclonic) or warm (anticyclonic) eddies seems to decrease or increase $pCO_{2,sw}$, respectively, which reflects vertical mixing and the effect of temperature on $pCO_{2,sw}$ [*Hood et al*., 2001; *Chen et al*., 2007]. The sea-air exchange of CO_2, is also believed to be greatly affected by tropical cyclones both locally [*Bates et al*., 1998; *Perrie et al*., 2004; *Nemoto et al*., 2009] and globally [*Levy et al*., 2012].

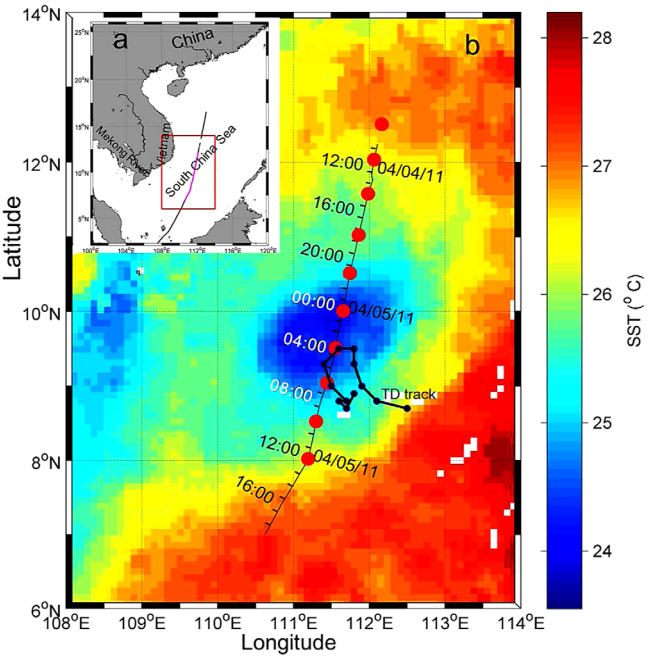

Figure 1. (a) Location of the study area in South China Sea. The red box identifies the enlarged area in Figure 1b, and the black line indicates the ship's track (the pink part within the red box corresponds to the data track in Figure 1b). (b) Area where data and samples were obtained from the ship between 4 and 6 April 2011. The ship track extends from 13°N to 7°N; red circles: sites of XBT casts; thick black line: tropical depression (TD) track. The base map shows SST on 4 April 2011.

Different processes may alter the upper-ocean environment through their combined effects. For example, the passage of a tropical cyclone is accompanied by strong winds that may cause Ekman pumping divergence, which may strengthen an already existing eddy-driven upwelling [*Large and Crawford*, 1995; *Obata et al.*, 1996], and preexistence of an eddy modifies physical condition in the upper ocean, which influences the extent of its response to a tropical cyclone [*Zheng et al.*, 2008; *Liu et al.*, 2009]. Responses of $pCO_{2,sw}$ and sea-air CO_2 exchange to such concurrent events are not well studied. The present work examines changes in $pCO_{2,sw}$ and the sea-air CO_2 flux caused by the passage of a tropical depression (TD) in an area of the South China Sea where a cold eddy preexisted and there was strong rainfall. The objective is to characterize the roles of concurrent episodic events, i.e., the passage of a TD, eddy-driven uplifting, and freshwater from rain, on the local exchange of CO_2 between the atmosphere and the ocean.

2. Data and Methods

2.1. In Situ Data Sets and Satellite Products

2.1.1. Tropical Depression Data

Our study was conducted in South China Sea (SCS, Figure 1a). Tropical Depression ONE, the object of the present study, was classified as a TD according to the Saffir-Simpson hurricane wind scale. It originated at 00 UTC on 2 April 2011 at 9.3°N, 111.3°E, and traveled slowly until it died out at 06 UTC on 3 April at 9.1°N, 111.7°E (black line in Figure 1b). The TD lasted a total of about 30 h, and the maximum wind speed was ~15.5 m s^{-1} at both 12 and 18 UTC on 2 April. The depression moved slowly, and its maximum translation speed was 1.63 m s^{-1}.

The TD data used in this study correspond to the best-track data of the U.S. Joint Typhoon Warning Centre (JTWC, http://www.usno.navy.mil/JTWC/). The best-track data include the location and intensity (i.e., maximum 1 min mean sustained 10 m wind speed) of the TD center at 6 h intervals, the wind radius, and the radii of specified winds (i.e., 17, 25, 33, and 51 m s^{-1}) for the four quadrants.

2.1.2. Satellite Products

Ocean surface conditions and physical processes before, during, and after the TD passage were determined from remotely sensed products. Data were averaged weekly from 24 to 30 March 2011 (pre-TD), 31 March 2011 to 6 April 2011 (during-TD), and 7 to 13 April 2011 (after-TD) and daily from 1 March 2011 to 30 April 2011. The products include: optimally interpolated SST and sea surface wind velocity and direction (~10 m above the sea surface) of ASCAT from remote sensing systems (http://www.remss.com/); rainfall from Tropical Rainfall Measuring Mission (TRMM); merged sea level anomaly (SLA), produced and distributed by Archiving, Validation and Interpretation of Satellite Oceanographic data (AVSIO, http://www.aviso.oceanobs.

com/); and 10 day composite sea surface salinity (SSS), from the "Centre Aval de Traitement des Données SMOS" (CATDS). The spatial resolution of these satellite products was 25 km, except for the SST (9 km).

2.1.3. Ship-Collected Data

We participated in a research cruise organized by the South China Sea Institute of Oceanology, Chinese Academy of Sciences in the SCS and the East Indian Ocean from 30 March 2011 to 18 May 2011. For the present study, we focus on the data collected about 2 days after the passage of the TD, from 4 to 6 April, i.e., from 7.0°N to 13°N (Figure 1b). The $pCO_{2,sw}$ was determined using an automated flowing pCO_2 measuring system (GO8050, General Oceanics Inc., USA), which is widely used on ships and on a variety of at-sea platforms for measuring $pCO_{2,sw}$ [*Zhai et al*., 2005; *Pierrot et al*., 2009]. The standard error between measured values and standard gases was $<1\%$.

During the entire cruise, seawater was pumped from a bow intake located $\sim$5 m below the sea surface: SST and SSS were measured and recorded every 5 s with a SEACAT CTD (SBE21, Sea-Bird Co.), the percent saturation of dissolved oxygen (DO) and chlorophyll *a* (Chl*a*) concentration was measured and recorded every 3 min with a Yellow Springs Instrument (YSI6600), and $pCO_{2,sw}$ (previous paragraph) was measured during 70 s/record; the SST, SSS, and $pCO_{2,sw}$ records were averaged over 3 min. Using the same GO8050 as for $pCO_{2,sw}$, the concentration of atmospheric pCO_2 ($pCO_{2,air}$) was measured every 2 h on air pumped from a bow intake located at the prow $\sim$10 m above the water surface; after removing water vapor, it was corrected to 100% humidity at in situ SST and SSS for the sea-air flux estimation. Depth profiles of temperature were obtained with Expendable Bathythermographs (XBT), which were dropped every 50 km along the ship's track (Figure 1b, red dots). Current speed and directions of each layer (8 m apart; first depth: 22 m) down to 500 m were obtained using an Acoustic Doppler Current Profiler (ADCP).

2.2. Calculations

2.2.1. Mixed Layer Depth and Ekman Pumping Velocity

Mixed layer depth (MLD) was estimated from the XBTs temperature profiles. The MLD was defined as the depth where the temperature was 0.5°C lower than the mean value in the upper 10 m of the water column [*Obata et al*., 1996].

Wind stress curl (τ) and Ekman pumping velocity (EPV) were calculated with daily satellite wind data as follows [*Price*, 1981]:

$$\tau = \rho_a * C_d * u_{10}^2 \tag{1}$$

$$\mathrm{EPV} = -Curl_z\left(\frac{\tau}{f * \rho_\omega}\right) \tag{2}$$

where ρ_w is the density of seawater (1020 kg m^{-3}), f is the Coriolis parameter, ρ_a is the density of air (1.25 kg m^{-3}), C_d is the drag coefficient (2.6×10^{-3}), and u_{10} is the wind speed 10 m above the sea level.

2.2.2. Character of the Cold-Core Eddy

The center of the cold eddy was identified by searching for the local SLA minimum. The closed contour of SLA $= -5$ cm around the eddy center defined the eddy edge, and the moving speed of the eddy was the rate at which the eddy center traveled [*Hu et al*., 2011; *Zhou et al*., 2013].

Eddy kinetic energy (EKE) was estimated as one half the sum of the squared eddy velocity components

$$\mathrm{EKE} = 0.5\ \left(u^2 + v^2\right) \tag{3}$$

where u and v are the zonal and meridian geostrophic velocity components, with positive values directed eastward (x) and northward (y), respectively, which were calculated from the SLA gradients as

$$u = -\frac{g}{f}\frac{\partial(SLA)}{\partial y},\quad v = \frac{g}{f}\frac{\partial(SLA)}{\partial x} \tag{4}$$

where g is the gravitational acceleration.

2.2.3. Sea-Air CO_2 Flux Estimation

The net sea-air CO_2 flux (F) was estimated using the sea-air pCO_2 difference and the sea-air gas transfer rate [*Liss*, 1973]:

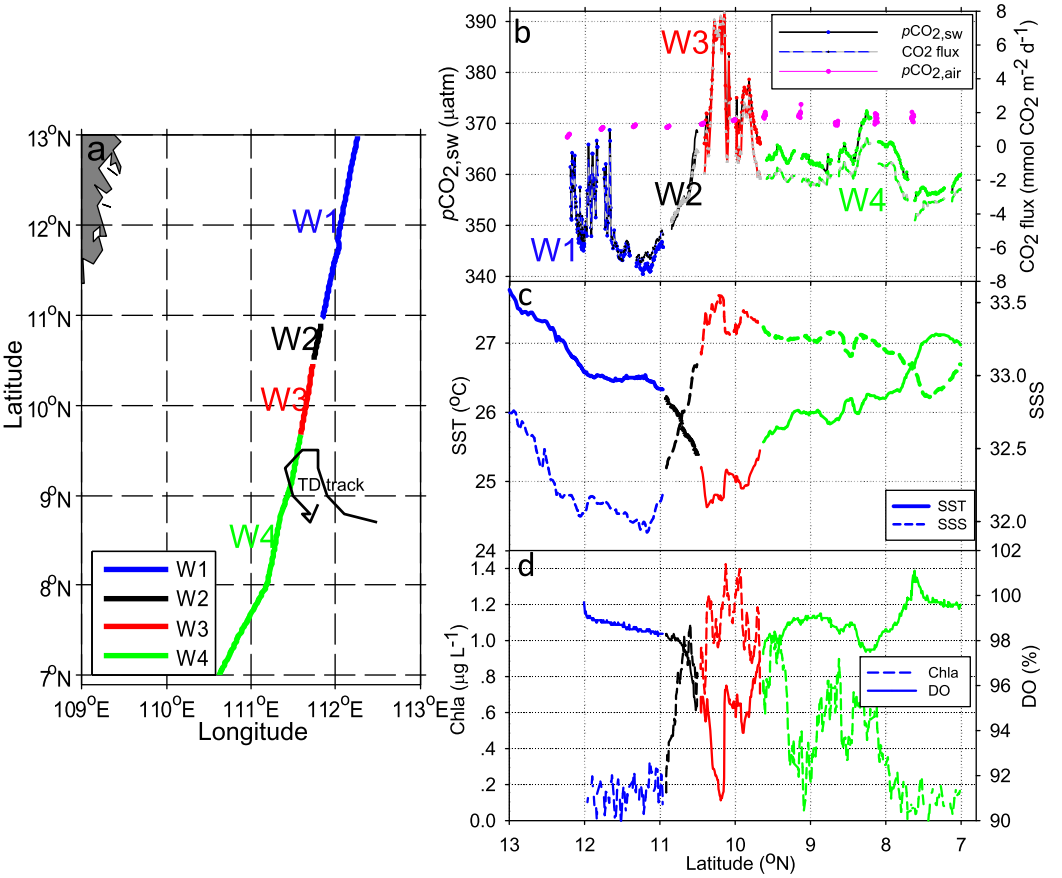

Figure 2. (a) Spatial distribution of the four water masses along the ship track: W1, W2, W3, and W4 (same color code as in Figure 3). Latitudinal variations of continuous shipboard measurements: (b) $pCO_{2,sw}$, $pCO_{2,air}$, and sea-air CO_2 flux, (c) SST and SSS, and (d) DO and Chl*a*.

$$F = k * K_H * (pCO_{2,sw} - pCO_{2,air}) \quad (5)$$

where k is the gas exchange coefficient and K_H is the solubility of CO_2 in seawater [*Weiss*, 1974]. Wanninkhof's equation was used to compute k [*Wanninkhof*, 1992]:

$$k = f_c * u_{10}^2 * (S_c/660)^{-0.5} \quad (6)$$

where f_c is a proportional coefficient (0.39 used in the present study), u_{10} is the wind speed 10 m above sea level, and S_c is the Schmidt number for CO_2 in seawater. Hence, positive F corresponds to a flux from ocean to atmosphere and negative F to a flux from atmosphere to ocean, indicating that the ocean is a sea-air CO_2 source or sink, respectively.

3. Results

3.1. Shipboard-Measured $pCO_{2,sw}$ and Other Characteristics

3.1.1. Sea-Surface Physical and Biogeochemical Observations

Using the sea-surface variables measured from the ship on 4 and 5 April, two clusters of dots with extreme characteristics could be identified on the SST-SSS and $pCO_{2,sw}$-SSS scatter diagrams (Figures 3a and 3b; corresponding latitudes from Figure 2a): W1 ("W" for water mass), with very low SSS (<32.8), low $pCO_{2,sw}$ (<368 μatm), and high SST (>26.5°C) from 10.96°N to 12.98°N, and W3, with relatively high SSS (>33.1), $pCO_{2,sw}$ (>366 μatm), and low SST (<25.5°C) from 9.67°N to 10.50°N. The characteristics of the other two water masses (W2 and W4) were distributed linearly between the two extreme clusters (Figures 3a and 3b and Table 1), and their latitudes were 10.50–10.96°N and 7.00–9.67°N, respectively. The highest $pCO_{2,sw}$, SSS, and Chl*a*, and lowest SST and DO occurred in W3 at ~10.2°N (Figures 2b–2d). The SST-SSS, $pCO_{2,sw}$-SSS, $pCO_{2,sw}$-DO, and $pCO_{2,sw}$-Chl*a* diagrams of the four water masses (Figure 3) showed that in W1

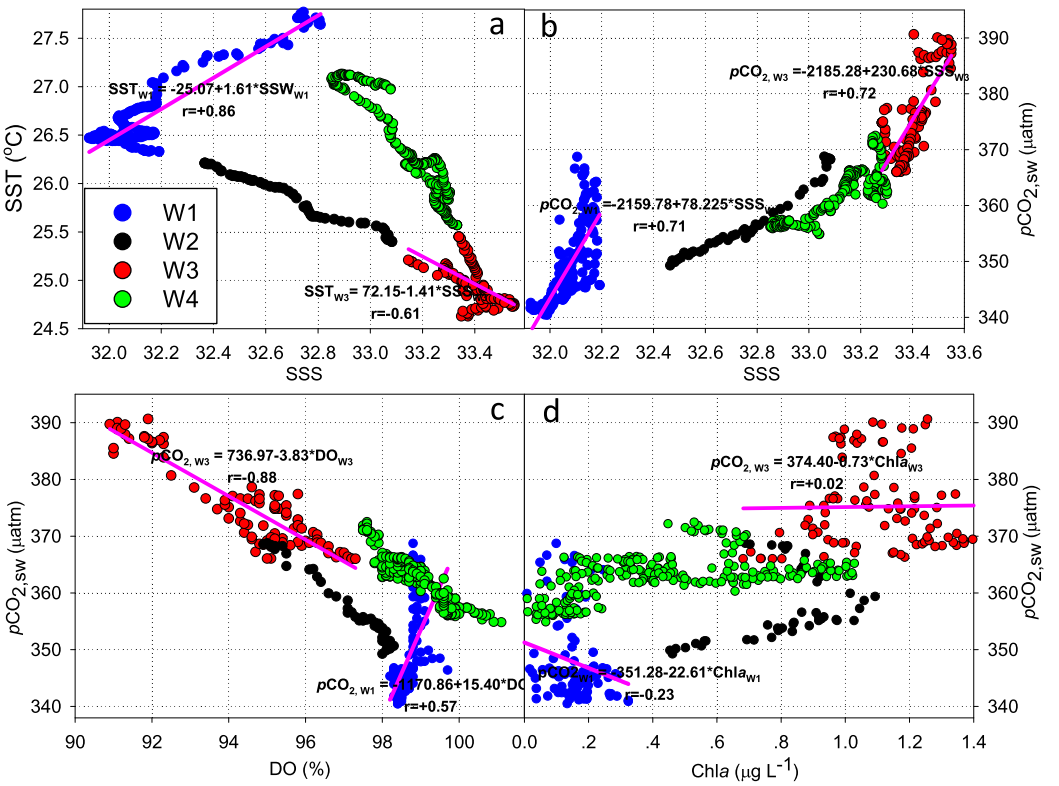

Figure 3. Scatter diagrams of variables determined in surface water: (a) SST versus SSS, (b) SSS versus $pCO_{2,sw}$, (c) DO versus $pCO_{2,sw}$, and (d) Chl*a* versus $pCO_{2,sw}$. The blue, black, red, and green dots correspond to water masses W1, W2, W3, and W4, respectively.

(blue dots), SSS was strongly correlated with SST (r = +0.86, N = 216, p <0.001), and $pCO_{2,sw}$ was strongly correlated with both SSS and DO (r = +0.71 and +0.57, N = 173 and 123, p <0.001 and 0.001, respectively) and only weakly correlated with Chl*a* (r = −0.23, N = 123, p = 0.013). In W3 (red dots), SSS was strongly correlated with SST (r = −0.61, p < 0.001), and $pCO_{2,sw}$ was strongly correlated with both SSS and DO (r = 0.72 and −0.88, N = 95 and 95, p < 0.001 and 0.001, respectively) and not correlated with Chl*a* (r = 0.02, N = 95, p = 0.85).

3.1.2. Vertical Changes in Isotherm Depths and Currents Along the Ship Track

Variations in the depths of isotherms (Figure 4a, based on XBTs) show that the mean MLD (Table 1) was deepest in W1 (41 ± 7 m), shallowest in W3 (25 ± 3 m), and intermediate in W2 and W4 (34 ± 18 and 36 ± 5 m, respectively). There were two domes of isotherms, i.e., one centered on 11.57°N (W1) with MLD of 32 m and the other on 10.52°N (W2–W3) with MLD of 22 m. Temperatures in the W1 and W3 areas were lower than elsewhere at all depths down to 80 m, especially at 10.20°N, and the 25°C isotherm in the W3 area reached the sea surface up from a depth of ~40 m. Changes in current directions at depth suggested rotating movements in two zones: a small one in the center of the W1 area (~11.6°N; see the currents at 54 and 70 m), and a larger one in the W3 area (~10.3°N; see the currents at 102, 118, 134, and 150 m (Figure 4b).

Table 1. Temporal and Spatial Distributions and Characteristics (Mean ± Standard Deviation) of the Four Water Masses

Water Mass	Sampling Dates	Location (°N)	Sample Size	MLD (m)	SST (°C)	SSS	DO (%)	Chl*a* (μg L^{-1})	$pCO_{2,sw}$ (μatm)	Sea-Air CO_2 Flux (mmol CO_2 m^{-2} d^{-1})
W1	4 Apr 2011, 12:50–5 Apr 2011, 02:33	10.96–12.98	216	41 ± 6	26.7 ± 0.3	32.13 ± 0.16	99 ± 0	0.2 ± 0.1	349 ± 7	−4.7 ± 1.8
W2	4 Apr 2011, 02:34–5 Apr 2011, 05:23	10.50–10.96	54	34 ± 18	25.8 ± 0.3	32.73 ± 0.23	97 ± 1	0.7 ± 0.2	376 ± 6	−2. 7 ± 1.3
W3	5 Apr 2011, 05:25–5 Apr 2011, 11:02	9.67–10.50	95	25 ± 3	25.0 ± 0.2	33.38 ± 0.09	95 ± 2	1.1 ± 0.2	376 ± 8	1.2 ± 3.1
W4	5 Apr 2011, 11:03–6 Apr 2011, 02:25	7.00–9.67	300	36 ± 5	26.3 ± 0.5	33.16 ± 0.14	99 ± 1	0.4 ± 0.3	362 ± 4	−2.0 ± 1.0

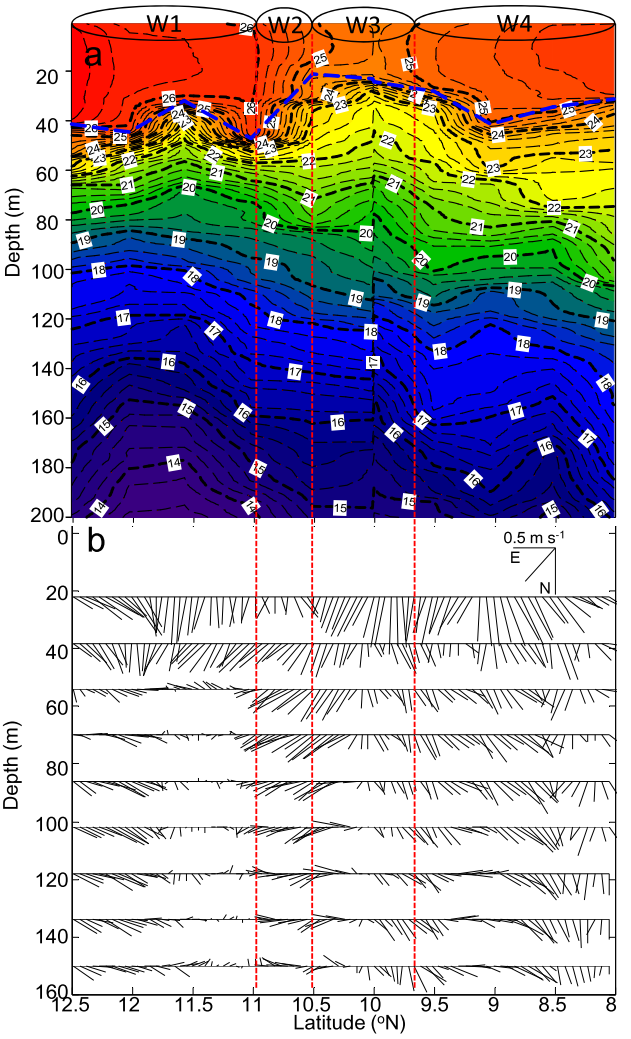

Figure 4. Latitudinal variations in depths of isotherms and in currents at various depths. (a) Isotherms derived from XBTs. The blue dashed line identifies the MLD. (b) Current directions at depths of 22, 38, 54, 70, 86, 102, 118, 134, and 150 m. The red vertical dashed lines identify the zonal distributions of the four water masses.

3.2. Changes in the Upper Ocean in Relation With TD Characteristics From Space

3.2.1. Wind, Rain, and SST Before, During, and After the TD

One week composite satellite images corresponding to before, during, and after the passage of the TD show a clear wind vortex during the passage of the TD, and corresponding higher EPV relative to before or after TD passage (Figure 5a). Based on the daily wind images (not shown), the maximum wind speed and EPV reached 11.7 m s^{-1} and 6 $\times$ 10^{-5} m s^{-1}, respectively, on 2 April 2011 when the depression started. Precipitation started before the arrival of the TD, and lasted from 21 March to 5 April, period during which the rainfall over the whole sampling area was about 300 mm, with the average heaviest daily value of 34 mm on 30 March (Figures 5b and 6a). The average daily rainfall in W1 and W3 was very heavy 1 week before and during the passage of the TD, with maxima on 24 March (89 mm) and 3 April (105 mm), respectively (Figure 6a). There was a general decrease of SST during the passage of the TD, the largest cooling occurring to the left (i.e., east) of the TD track (Figure 5c). The greatest SST decrease ($\sim$3.2°C lower than the monthly averaged value) occurred at 10.00°N, 111.25°E on 4 and 5 April (satellite images not shown).

3.2.2. Temporal Changes in a Preexisting Cyclonic Eddy

Negative SLA combined with anticlockwise geostrophic currents indicate the presence of a cyclonic eddy before the passage of the TD, with minimum SLA ($-$11 cm) at 11.50°N, 111.75°E (Figure 5d, left). During the passage of the TD, the eddy strengthened, and its center shifted to the southeast (minimum SLA of $-$14 cm at 11.50°N, 111.5°E, Figure 5d, middle) toward the SST cooling core (10.00°N, 111.25°E, Figure 5c, middle). Lower minimum SLA ($-$15 cm) and continuous shifting of the center of the eddy (11.25°N, 111.25°E) to the southeast were observed 1 week after the passage of the TD (Figure 5d, right). The eddy disappeared 2 weeks after the TD (i.e., late April, not shown).

Three indicators of the cyclonic eddy obtained from daily SLA images showed major changes as the TD passed over the region, i.e., the minimum SLA value, used as index of cold eddy intensity; EKE; and moving speed, U_h (Figure 6b). Minimum SLA started to decrease on 2 April below its usual minima in a previous week, and reached its lowest value ($-$16 cm) on 10 April (Figure 6b). Values of EKE and eddy moving speed started to increase on 4 and 2 April, respectively, and reached their maximum values of 0.3 m^2 s^{-2} and 1.9 $\times$ 10^{-4} m s^{-1} on 10 and 7 April, respectively.

3.2.3. Horizontal Variations in Sea Surface Salinity

Satellite images of 10 day averaged SSS data from CATDS show two zones of low SSS ($<$32.5) before the TD (22–31 March, Figure 7a): the first was centered on 12°N, 112°E, which coincided with ship-sampled

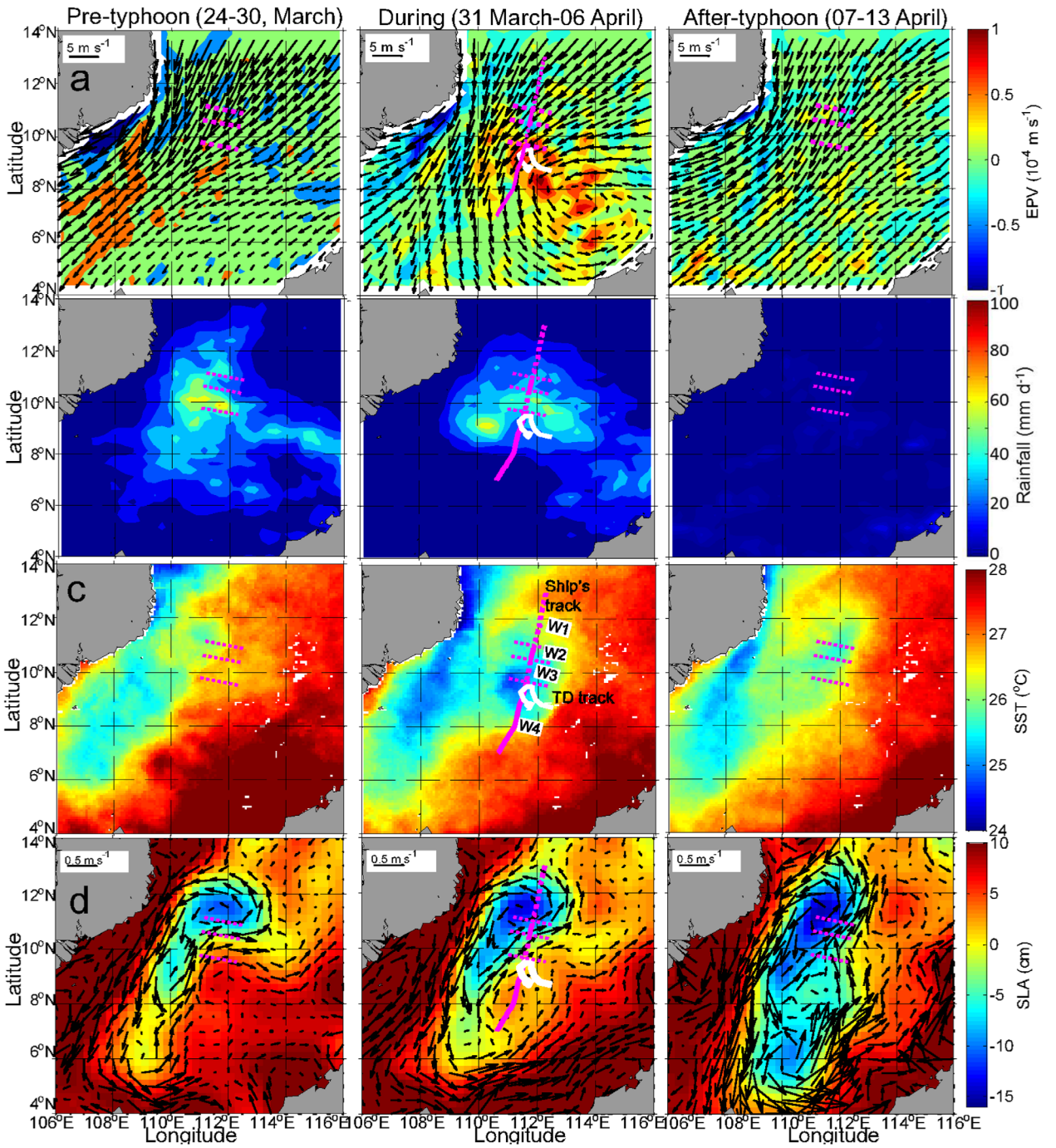

Figure 5. Weekly averaged satellite images of (a) surface wind vectors and Ekman pumping velocity (EPV), (b) rainfall, (c) SST, and (d) surface geostrophic currents and sea level anomaly. (first column) One week before the TD passage (from 23 to 30 March 2011); (second column) during the TD passage and after, i.e., ship sampling (from 31 March 2011 to 6 April 2011); (third column) after the TD (from 7 to 13 April 2011). In all plots, the three horizontal dotted pink lines indicate the borders between the four water masses (W1, W2, W3, and W4); these are identified in the center plots, where the ship's track is also shown. The thick white line in the central plots corresponds to the TD's track.

water at W1 (Figure 2a, mean SSS value of 32.09 from 10.96°N to 12.97°N), and the second was centered on ~9°N, 111°E, close to Mekong River and to ship-sampled water at W3 (Figure 2a, mean SSS value of 32.09 from 9.67°N to 10.50°N). The second low-SSS zone covered a surface area larger than the first, and the two zones seemed to be interconnected by a tongue of low-SSS water. The two low-SSS zones were not present on the next 10 day image, and SSS in the two previously low-SSS zones was >33.00 (1–10 April, Figure 7b).

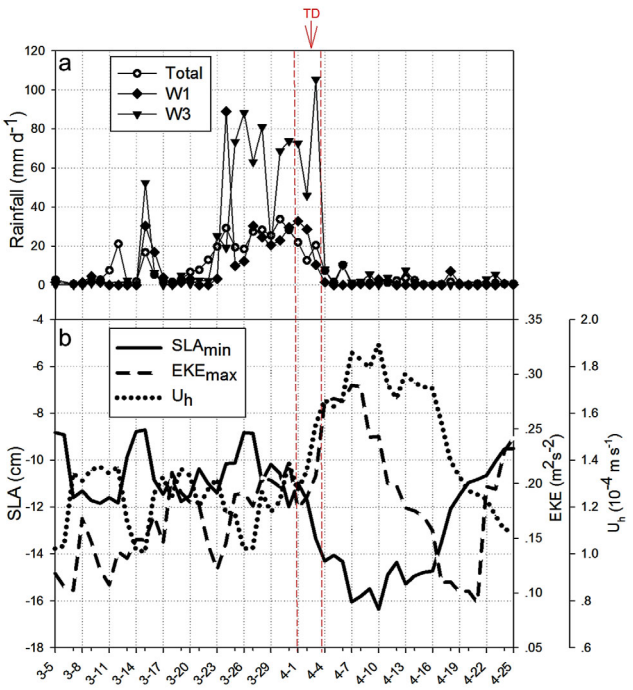

Figure 6. Temporal changes from 5 March 2011 to 25 April 2011 in (a) average rainfall over the whole sampling area (total), and in W1 and W3 along the sampling track, and (b) three cold-eddy indicators: minimum SLA (SLA_{min}), maximum EKE (EKE_{max}), and current velocity (U_h). The red vertical dash lines correspond to the beginning and the end of the passage of the TD.

4. Discussion

4.1. Presence of a Cold Eddy

The water column under W1 (i.e., north of 10.96°N) showed rotating movement, associated weak dome of isotherms, and relatively shallow MLD (Figure 4). At the sea surface, negative SLA combined with anticlockwise geostrophic currents indicated the presence of a cyclonic eddy (Figure 5d). All these characteristics point toward the presence of a cold cyclonic eddy [*Wang et al*., 2003; *Hu et al*., 2011] before, during, and after the passage of the TD. However, there was no corresponding cold water at the surface (Figure 5c), indicating that the upward movement of underlying water associated with the cold eddy was not strong enough to bring these water to the surface as confirmed by the observation that the 26°C isotherm had not reached the surface on 4 April, 1 day after the passage of the TD (Figure 4a). This was perhaps because the low SSS in W1 created a density gradient that was too strong to be broken by the uplifting generated by the cold eddy.

4.2. Four Surface Water Masses

Four water masses with different characteristics were observed from the ship at sea surface (Figures 2 and 3).

First, W1 water mass covered a wide area north of 10.96°N (Figure 2a). It was characterized by high SST, low SSS, low $pCO_{2,sw}$, high DO, and low Chl*a* (Table 1). Its SST and $pCO_{2,sw}$ were highly correlated with SSS

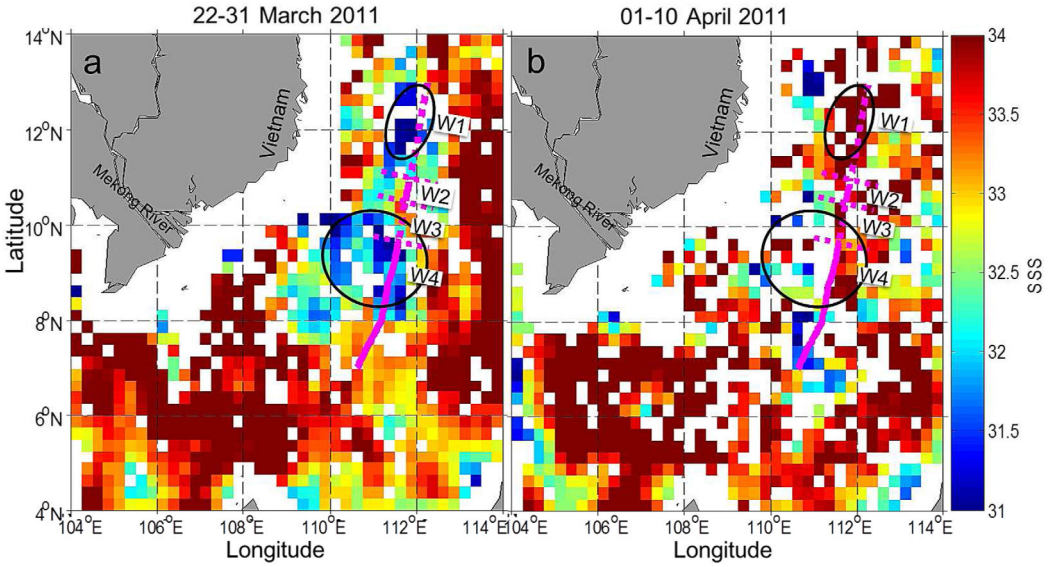

Figure 7. Two 10 day composite SSS distributions from CATDS data sets (a) 22–31 March and (b) 1–10 April. In the two plots, the three horizontal dotted pink lines indicate the borders between the four water masses (W1, W2, W3, and W4); these are identified in both plots, where the ship's track is also shown. The two ellipses identify two main areas of lower salinity water.

(r = +0.86 and +0.71, respectively, Figures 3a and 3b). Water mass W1 corresponded to the smallest and northernmost of the two interconnected low-SSS zones that were present before the passage of the TD and extended between ~8°N and ~13°N (Figure 7a). Taking the SSS of W4 water mass (33.16, Table 1) as a typical value for the area (see below), the SSS of W1 water (32.13) would represent the mixing of 31 parts of W4 water with one part of freshwater. There were at least two possible sources for this freshwater, i.e., the Mekong River, located ~360 km away (Figure 1), and the rain that fell on the region before ship sampling, i.e., from 24 March to 3 April (Figure 5b). The low-SSS W1 water is further discussed in the next section.

Second, water mass W3 (9.67–10.50°N) covered a much smaller area than W1 (Figure 2a). They were characterized by low SST, high SSS, high $pCO_{2,sw}$, low DO, and high Chl*a* (Table 1), i.e., the exact opposite of water mass W1. Its SSS and DO were correlated with $pCO_{2,sw}$ moderately and highly, respectively (r = 0.72 and −0.88, respectively, Figures 3b and 3c). The water column under W3 showed a large rotating movement, strong dome of isotherms and shallow MLD (Figure 4), and the sea surface in W3 presented, during the passage of the TD, high EPV corresponding to a strong wind vortex, and a large area of cold water (Figures 5a and 5c). All these characteristics point toward the occurrence of wind-driven uplifting of deeper water associated with the passage of the TD. The low temperature of surface water in W3 (mostly <25°C) suggests that these came from as deep as 40 m (Figure 4a), by Ekman pumping in response to the winds associated with the passage of the TD (Figures 4a and 5a). Hence, the characteristics of surface water in W3 would reflect the uplifting to the surface of subsurface water with low SST, high SSS, high $pCO_{2,sw}$, low DO, and high Chl*a* caused by the passage of the TD. The first four characteristics are those expected for water uplifted from depth, and high Chl*a* indicates the presence of a deep Chl*a* maximum, as predicted by a model to occur at a depth of 40–60 m [*Sasai et al*., 2013] and as observed at ~50 m during the spring intermonsoon season [*Wang and Tang*, 2014].

Third, water mass W2 (10.50–10.96°N) covered a small area between W1 and W3 (Figure 2a). Its characteristics were intermediate between those of the two neighboring zones (Figure 3 and Table 1). This indicates that water mass W2 likely resulted from horizontal mixing between water mass W1, which was influenced by freshwater, and water mass W3, which was uplifted from depths ≤40 m, as result of the passage of the TD.

Fourth, water mass W4 covered a large area south of W3 (i.e., south of 9.67°N, Figure 2a), its characteristics extended over a larger area of W3 (Figure 3 and Table 1). The W4 water had mean SST, SSS, $pCO_{2,sw}$, DO, and Chl*a* of 26.3°C, 33.16, 362 μatm, 99%, and 0.4 μg L^{-1}, respectively (Table 1), which is interpreted as resulting from horizontal mixing between water mass W3, uplifted during the passage of the TD, and "normal" surface SCS water. The extreme W4 values correspond to those found in the literature for the SCS in March-April [*Zhai et al*., 2005, 2009, 2013].

4.3. Low Surface $pCO_{2,sw}$: Freshwater Due to Rainfall

In W1, the low-SSS water (32.13 ± 0.16) had low $pCO_{2,sw}$ (349 ± 7 μatm) and sea-air CO_2 flux (−4.7 ± 1.8 mmol CO_2 m^{-2} d^{-1}) (Figure 2b). It was explained in the previous section that, taking the SSS of W4 water (33.16, Table 1) as a typical value for the area, the SSS of W1 water would represent the mixing of 31 parts of W4 water with one part of freshwater. There were two possible sources considered for this freshwater, i.e., the Mekong River and the rain that fell on the region before ship sampling, i.e., from 24 March to 3 April (Figure 5b).

Water from the Mekong River is characterized by high pCO_2 (up to >1500 μatm [*Li et al*., 2013]) and high nutrients (e.g., $NO_3 + NO_2$ = 12.4 μmol L^{-1} [*Grosse et al*., 2010]). Given that the pCO_2 of Mekong water is much higher than that of SCS (e.g., W4, 362 μatm, Table 1), mixture of the two water masses should have resulted in higher $pCO_{2,sw}$ than W4, which is contrary to what was observed in W1 (i.e., $pCO_{2,sw}$ = 349 μatm, Table 1). Similarly, the high nutrients in Mekong water should have caused relatively high Chl*a* in W3, which is contrary to observation there (i.e., Chl*a* = 0.2 μg L^{-1}, Table 1). Hence, it is unlikely that water from the Mekong River contributed much to the characteristics of W1.

Concerning the possible effect of rainwater, one must first consider the characteristics of SCS water, i.e., W4. Given the SSS and $pCO_{2,sw}$ of W4, the total alkalinity (TA) [*Lee et al*., 2006] and dissolved inorganic carbon (DIC) [*DOE*, 1994] of this water were 2199 and 1883 μmol kg^{-1}, respectively. Mixing 31 parts of W4 water with one part of rainwater would have added no or little TA or DIC [*Turk et al*., 2010; *Cao et al*., 2014], so that

TA and DIC of the mixture, given its S = 32.12, would have been 2130 and 1824 μmol kg^{-1}, respectively, and its $pCO_{2,sw}$ would thus have been 351 μatm. The latter value is very close to the actual $pCO_{2,sw}$ observed in W1 (349 μatm). Furthermore, the (mean) 0.3 m of rain that fell on the W1 area from 24 March to 3 April (Figure 6a) could have diluted a thickness of 0.3 m $\times$ (31 + 1) = 9.5 m of seawater from a salinity of 33.16 down to 32.13, which is more than enough to account for the SSS measured on board the ship 5 m below the sea surface. Hence, the observed characteristics of W1 could be explained by the rain that fell on the W1 area between 24 March and 3 April.

The presence of a cold eddy in W1 (see above) could have suggested that the uplifting to the surface of deeper, more saline, and CO_2-riched water would have resulted in higher $pCO_{2,sw}$ and sea-air CO_2 flux as reported in other studies [*Chen et al*., 2007; *Bond et al*., 2011]. However, this was not the case in W1 because the uplifting of deeper water there was not strong enough to bring this deep water to the surface, contrary to W3 where the observed high SSS reflected strong upward water movement (Figure 4a). However, on the 10 day satellite composite image (Figure 7b, 1–10 April), SSS in W1 is very high (>34), possibly because the eddy-driven uplifting, which may have been strengthened by the passage of the TD (Figure 6b), finally brought deeper, salty water to the surface after the passage of the ship on 4–5 April.

4.4. High Seawater $pCO_{2,sw}$: Passage of the TD

High $pCO_{2,sw}$ (376 $\pm$ 8 μatm) and sea-air CO_2 flux (2.0 $\pm$ 3.1 mmol CO_2 m^{-2} d^{-1}) were observed in W3 (Table 1), which was the area directly affected by the passage of the TD. There, SST and DO were low, and SSS and Chl*a* were high (Table 1), and SSS was correlated with SST (moderately), and $pCO_{2,sw}$ with SSS (moderately) and DO (highly) (Figure 3). These characteristics and relationships indicate mixing of cold, salty, and DO-poor subsurface water with the surface water, hence the uplifting of deeper water to the surface. In addition, the MLD and the isotherms formed a dome, the 25°C isotherm reached the sea surface, and changes in current direction at depth suggested rotating movement over the W3 area (Figure 4b). All these reinforce the explanation of surface water characteristics influenced by the uplifting of deeper water with low temperature and DO, and high salinity, $pCO_{2,sw}$, and Chl*a*. The cause of the uplifting would have been the winds associated with the passage of the TD (Figure 4a), and the positive sea-air CO_2 flux, a consequence of the influx of deeper water with high $pCO_{2,sw}$ into the surface layer.

The above uplifting is consistent with the average EPV calculated from satellite wind data and the time lag between the passage of the depression and the ship's observations, i.e., $\sim 6 \times 10^{-5}$ m s^{-1} and 2 days (i.e., 1.7×10^5 s). Multiplying these two values provides a simple estimation of the wind-driven uplifting, i.e., $\sim$10.4 m, which is comparable to the observed elevation of the MLD by 11 m (i.e., the difference between MLD in W3 and W4, Table 1).

A very high Chl*a* concentration (1.1 $\pm$ 0.2 μg L^{-1}, Table 1) was observed in W3 after the TD passage. This could have been caused by two different mechanisms. On the one hand, the strong winds that accompany a tropical depression cause vertical mixing of the water column, which entrains deeper, nutrient-rich water into the euphotic zone [*Hung and Gong*, 2011; *Chung et al*., 2012; *Chen et al*., 2013]. These nutrients may trigger a rapid increase in phytoplankton biomass (mostly picophytoplankton in the SCS [*Ning et al*., 2004; *Hung et al*., 2009]). On the other hand, the upwelling and vertical mixing induced by a tropical cyclone as a result of strong winds may transport deeper water with high Chl*a* to the surface, as reported in other areas of the SCS [*Lin et al*., 2003; *Zhao et al*., 2009; *Ye et al*., 2013] and is consistent with the presence of a deep Chl*a* in the sampling area at a depth of 40–60 m (see above). This can cause high surface Chl*a* concentration. Given the lack of relationship between Chl*a* and $pCO_{2,sw}$ in W3 (r = +0.02, Figure 3d), the high surface Chl*a* there did not likely result from local photosynthesis but instead reflected the uplifting of deeper water with high Chl*a* concentration, especially considering that the 25°C isotherm in the W3 area reached the sea surface up from a depth of $\sim$40 m (Figure 4a). This mechanism assumes that a deep Chl*a* maximum was present in the W3 sampling area before the passage of the TD.

4.5. Effects on Local CO_2 Exchange

The extent of the cold eddy increased during the passage of the TD, and included the TD-affected area after the TD had passed (Figure 5d, middle and right). This indicates that the two areas were somehow related:

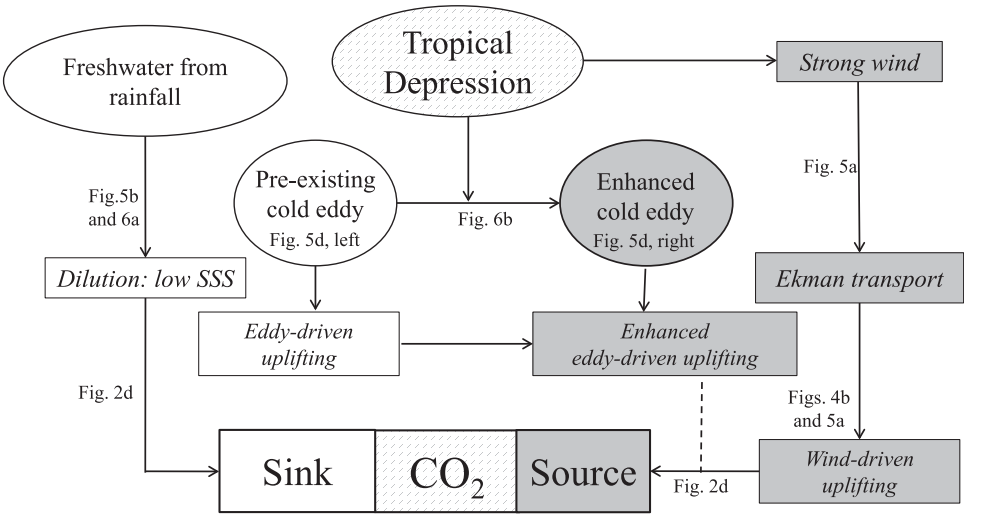

Figure 8. Conceptual diagram illustrating the mechanisms by which dilution by freshwater and the passage of the TD caused the negative and positive sea-air CO_2 fluxes postulated before the passage of the TD and observed after the TD had passed, respectively. The solid lines correspond to physical mechanisms and the dotted line to a hypothetical effect. The different figures on which the mechanisms are based in the text are identified.

the possible connection and interaction between the two areas below the surface layer could have influenced the effect of the TD on sea-air CO_2 fluxes, although the only vertical data available (i.e., Figure 4) do not provide information on such processes.

Before the passage of the TD, the surface water above the cold eddy (W1 in Figure 2a) and the water that would later be affected by the TD (W3 in Figure 2a) had similar low SST and low SSS because they were both affected by freshwater (Figures 5c and 7). Hence, it is possible that these water masses also shared other properties, including low $pCO_{2,sw}$ and sea-air CO_2 flux. After the passage of the TD, the average sea-to-air CO_2 flux in W1 (above the cold eddy) and W3 (TD-affected water) were -4.7 ± 1.8 and 2.0 ± 3.1 mmol CO_2 m^{-2} d^{-1}, respectively, showing that the freshwater-invaded area was a regional sink for atmospheric CO_2, and the TD-affected water was a source. Assuming that the water properties of W3 were similar to those of W1 in late March, the passage of the TD would have transformed W3 water from an atmospheric CO_2 sink into a source. Under this assumption, the difference between the CO_2 flux in W3 before and after the passage of the TD could have been $\sim 4.7 + \sim 2.0 = 6.7$ mmol CO_2 m^{-2} d^{-1}, i.e., a 100% change compared to the average seasonal sea-air CO_2 flux in spring in the southern SCS (3.3 ± 0.3 mmol CO_2 m^{-2} d^{-1}, reported by *Zhai et al.* [2013]).

The process by which tropical cyclones influence CO_2 sea-air fluxes, is complex, as the piston velocity and $pCO_{2,sw}$ change in response to the high wind speeds and physical processes (e.g., mixing, cooling, and upwelling) caused by the cyclones [*Wanninkhof*, 1992; *Perrie et al.*, 2004; *Nemoto et al.*, 2009]. Contrary to some observed very high efflux of CO_2 caused by tropical cyclones (i.e., negative sea-air CO_2 flux [*Bates et al.*, 1998; *Perrie et al.*, 2004; *Nemoto et al.*, 2009]), the present study reports high $pCO_{2,sw}$ and positive sea-air CO_2 flux, i.e., an influx from atmosphere to ocean. This could be explained by two factors that are related to the special characteristics of the TD and the pre-TD ocean conditions in this study, (1) undersaturation of CO_2 prior to the TD due to dilution by freshwater and the preexisting cold eddy. In undersaturated CO_2 conditions, the instantaneous wind effect induced by the tropical cyclone and the postcyclone mixing effect add up [*Levy et al.*, 2012] to increase the CO_2 influx from the atmosphere into the ocean. (2) Slow translation speed of the TD. Translation speed is a key factor determining the response of the upper ocean to tropical cyclones because a slower translation speed corresponds to a longer residence time of the tropical cyclone over the area it influences [*Gierach and Subrahmanyam*, 2008; *Zhao et al.*, 2008; *Sun et al.*, 2010; *Lin*, 2012]. The maximum translation speed of the TD in the present case was 1.6 m s^{-1}, which is much less than the threshold between slow and fast-moving typhoons, i.e., 6 m s^{-1} [*Price*, 1981]. This could explain the observed large responses exhibited in this study by such physical characteristics as upwelling, MLD shoaling, and uplifting of deeper water into the surface layer.

5. Conclusions

This study showed how the passage of a TD over the SCS turned a sink for atmospheric CO_2, which was related to dilution by freshwater, into a source. The different mechanisms involved in the changes caused by freshwater and the passage of the TD are presented schematically in Figure 8, which indicates that the overall mechanism in the TD-affected area was that of wind-driven uplifting of deeper water. Our work showed that episodic events could have large effects on local sea-air CO_2 exchanges, and should be included in estimates of local CO_2 flux.

Acknowledgments

This study was supported by the following research projects awarded to D.L.T.: (1) National Natural Sciences Foundation of China (41430968, 31061160190, 40976091, 41106105); (2) Guangdong Sciences Foundation (2010B031900041, 8351030101000002); (3) Key Project of LTO (LTOZZ-1201), (4) China Petroleum & Chemical Corporation Project (313099), (5) scientific exchange agreement between the Chinese Academy of Sciences and the French Centre National de la Recherche Scientifique (D.L.T. and L.L). The authors thank the South China Sea Open Cruise, R/V Shiyan 3 (SCSIO, CAS), and are grateful to all members of the Research Center for Remote Sensing and Marine Ecology & Environment (RSMEE). We also acknowledge the use of Remote Sensing Systems for TMI-AMSRE sea-surface temperature and ASCAT wind data, GES DAAC for TRMM accumulated rainfall data, AVSIO for sea-level anomaly data, and the CATDS for SSS data. We are grateful to physical oceanographers provided advice on the interpretation of data, Ju Chen, Rongyu Chen, and Yunkai He from South China Sea Institute of Oceanology, Lei Wang from Tianjin University of Science and Technology, Kuanbo Zhou from Xiamen University, Louis Prieur from the Villefranche Oceanography Laboratory, France, and Anya Waite from University of Western Australia. We are also grateful to Jean-Pierre Gattuso from the Villefranche Oceanography Laboratory, France, for his advice on carbonate chemistry, and Gad Levy from NorthWest Research Associates, Inc., for his suggestion on English wording.

References

Bates, N. R. (2007), Interannual variability of the oceanic CO_2 sink in the subtropical gyre of the North Atlantic Ocean over the last 2 decades, *J. Geophys. Res.*, *112*, C09013, doi:10.1029/2006JC003759.

Bates, N. R., A. H. Knap, and A. F. Michaels (1998), Contribution of hurricanes to local and global estimates of air-sea exchange of CO_2, *Nature*, *395*(6697), 58–61, doi:10.1038/25703.

Bond, N. A., M. F. Cronin, C. Sabine, Y. Kawai, H. Ichikawa, P. Freitag, and K. Ronnholm (2011), Upper ocean response to typhoon Choi-Wan as measured by the Kuroshio Extension Observatory mooring, *J. Geophys. Res.*, *116*, C02031, doi:10.1029/2010JC006548.

Borges, A. V., and M. Frankignoulle (2001), Short-term variations of the partial pressure of CO_2 in surface waters of the Galician upwelling system, *Prog. Oceanogr.*, *51*(2–4), 283–302, doi:10.1016/S0079-6611(01)00071-4.

Cao, Z., M. Dai, W. Evans, J. Gan, and R. Feely (2014), Diagnosing CO_2 fluxes in the upwelling system off the Oregon coast, *Biogeosci. Discuss.*, *11*(5), 7389–7412, doi:10.5194/bgd-11-7389-2014.

Chen, F. Z., W. J. Cai, C. Benitez-Nelson, and Y. C. Wang (2007), Sea surface pCO_2-SST relationships across a cold-core cyclonic eddy: Implications for understanding regional variability and air-sea gas exchange, *Geophys. Res. Lett.*, *34*, L10603, doi:10.1029/2006GL028058.

Chen, K. S., C. C. Hung, G. C. Gong, W. C. Chou, C. C. Chung, Y. Y. Shih, and C. C. Wang (2013), Enhanced POC export in the oligotrophic northwest Pacific Ocean after extreme weather events, *Geophys. Res. Lett.*, *40*, 5728–5734, doi:10.1002/2013GL058300.

Chung, C. C., G. C. Gong, and C. C. Hung (2012), Effect of Typhoon Morakot on microphytoplankton population dynamics in the subtropical Northwest Pacific, *Mar. Ecol. Prog. Ser.*, *448*, 39–49, doi:10.3354/meps09490.

DOE (1994), *Handbook of Methods for the Analysis of the Various Parameters of the Carbon Dioxide System in Sea Water*, Version 2, edited by A. G. Dickson and C. Goyet, Washington, D. C.

Gierach, M. M., and B. Subrahmanyam (2008), Biophysical responses of the upper ocean to major Gulf of Mexico hurricanes in 2005, *J. Geophys. Res.*, *113*, C04029, doi:10.1029/2007JC004419.

Grosse, J., D. Bombar, N. D. Hai, N. N. Lam, and M. Voss (2010), The Mekong River plume fuels nitrogen fixation and determines phytoplankton species distribution in the South China Sea during low- and high-discharge season, *Limnol. Oceanogr. Methods*, *55*(4), 1668–1680, doi:10.4319/lo.2010.55.4.1668.

Hood, E. M., R. Wanninkhof, and L. Merlivat (2001), Short timescale variations of fCO_2 in a North Atlantic warm-core eddy: Results from the Gas-Ex 98 carbon interface ocean atmosphere (CARIOCA) buoy data, *J. Geophys. Res.*, *106*(C2), 2561–2572, doi:10.1029/1999JC000278.

Hu, J. Y., J. P. Gan, Z. Y. Sun, J. Zhu, and M. H. Dai (2011), Observed three-dimensional structure of a cold eddy in the southwestern South China Sea, *J. Geophys. Res.*, *116*, C05016, doi:10.1029/2010JC006810.

Huang, P. S., and J. Imberger (2010), Variation of pCO_2 in ocean surface water in response to the passage of a hurricane, *J. Geophys. Res.*, *115*, C10024, doi:10.1029/2010JC006185.

Hung, C.-C., and G. C. Gong (2011), Biogeochemical responses in the Southern East China Sea after typhoons, *Oceanography*, *24*(4), 42–51, doi:10.5670/oceanog.2011.93.

Hung, C.-C., G.-C. Gong, W.-C. Chung, W.-T. Kuo, and F.-C. Lin (2009), Enhancement of particulate organic carbon export flux induced by atmospheric forcing in the subtropical oligotrophic northwest Pacific Ocean, *Mar. Chem.*, *113*(1–2), 19–24, doi:10.1016/j.marchem.2008.11.004.

Hung, C.-C., et al. (2010), The effect of typhoon on particulate organic carbon flux in the southern East China Sea, *Biogeosciences*, *7*(10), 3007–3018, doi:10.5194/bg-7-3007-2010.

Large, W. G., and G. B. Crawford (1995), Observations and simulations of upper-ocean response to wind events during the ocean storms experiment, *J. Phys. Oceanogr.*, *25*(11), 2831–2852, doi:10.1175/1520-0485(1995)025.

Lee, K., L. T. Tong, F. J. Millero, C. L. Sabine, A. G. Dickson, C. Goyet, G. H. Park, R. Wanninkhof, R. A. Feely, and R. M. Key (2006), Global relationships of total alkalinity with salinity and temperature in surface waters of the world's oceans, *Geophys. Res. Lett.*, *33*, L19605, doi:10.1029/2006GL027207.

Levy, M., M. Lengaigne, L. Bopp, E. M. Vincent, G. Madec, C. Ethe, D. Kumar, and V. V. S. S. Sarma (2012), Contribution of tropical cyclones to the air-sea CO_2 flux: A global view, *Global Biogeochem. Cycles*, *26*, GB2001, doi:10.1029/2011GB004145.

Li, S., X. X. Lu, and R. T. Bush (2013), CO_2 partial pressure and CO_2 emission in the Lower Mekong River, *J. Hydrol.*, *504*, 40–56, doi:10.1016/j.jhydrol.2013.09.024.

Lin, I., W. T. Liu, C. C. Wu, G. T. F. Wong, C. M. Hu, Z. Q. Chen, W. D. Liang, Y. Yang, and K. K. Liu (2003), New evidence for enhanced ocean primary production triggered by tropical cyclone, *Geophys. Res. Lett.*, *30*(13), 1718, doi:10.1029/2003GL017141.

Lin, I. I. (2012), Typhoon-induced phytoplankton blooms and primary productivity increase in the western North Pacific subtropical ocean, *J. Geophys. Res.*, *117*, C03039, doi:10.1029/2011JC007626.

Lin, J. R., D. L. Tang, W. Alpers, and S. F. Wang (2014), Response of dissolved oxygen and related marine ecological parameters to a tropical cyclone in the South China Sea, *Adv. Space Res.*, *53*(7), 1081–1091, doi:10.1016/j.asr.2014.01.005.

Liss, P. S. (1973), Processes of gas-exchange across an air-water interface, *Deep Sea Res. Oceanogr. Abstr.*, *20*(3), 221–238, doi:10.1016/0011-7471(73)90013-2.

Liu, X. M., M. H. Wang, and W. Shi (2009), A study of a Hurricane Katrina-induced phytoplankton bloom using satellite observations and model simulations, *J. Geophys. Res.*, *114*, C03023, doi:10.1029/2008JC004934.

Mahadevan, A., A. Tagliabue, L. Bopp, A. Lenton, L. Memery, and M. Levy (2011), Impact of episodic vertical fluxes on sea surface pCO_2, *Philos. Trans. R. Soc. A*, *369*(1943), 2009–2025, doi:10.1098/rsta.2010.0340.

Nemoto, K., T. Midorikawa, A. Wada, K. Ogawa, S. Takatani, H. Kimoto, M. Ishii, and H. Y. Inoue (2009), Continuous observations of atmospheric and oceanic CO_2 using a moored buoy in the East China Sea: Variations during the passage of typhoons, *Deep Sea Res., Part II*, *56*(8–10), 542–553, doi:10.1016/j.dsr2.2008.12.015.

Ning, X., F. Chai, H. Xue, Y. Cai, C. Liu, and J. Shi (2004), Physical-biological oceanographic coupling influencing phytoplankton and primary production in the South China Sea, *J. Geophys. Res.*, *109*, C10005, doi:10.1029/2004JC002365.

Obata, A., J. Ishizaka, and M. Endoh (1996), Global verification of critical depth theory for phytoplankton bloom with climatological in situ temperature and satellite ocean color data, *J. Geophys. Res.*, *101*(C9), 20,657–20,667, doi:10.1029/96JC01734.

Perrie, W., W. Q. Zhang, X. J. Ren, Z. X. Long, and J. Hare (2004), The role of midlatitude storms on air-sea exchange of CO_2, *Geophys. Res. Lett.*, *31*, L09306, doi:10.1029/2003GL019212.

Pierrot, D., C. Neill, K. Sullivan, R. Castle, R. Wanninkhof, H. Luger, T. Johannessen, A. Olsen, R. A. Feely, and C. E. Cosca (2009), Recommendations for autonomous underway pCO_2 measuring systems and data-reduction routines, *Deep Sea Res., Part II*, *56*(8–10), 512–522, doi:10.1016/j.dsr2.2008.12.005.

Price, J. F. (1981), Upper ocean response to a hurricane, *J. Phys. Oceanogr.*, *11*(2), 153–175, doi:10.1175/1520-0485(1981)011.

Sasai, Y., H. Sasaki, and K. J. Richards (2013), Impact of physical processes on the phytoplankton blooms in the South China Sea: An eddy-resolving physical-biological model study, *Biogeosci. Discuss.*, *10*(1), 1577–1604, doi:10.5194/bgd-10-1577-2013.

Shih, Y. Y., J. S. Hsieh, G. C. Gong, C. C. Hung, W. C. Chou, M. A. Lee, K. S. Chen, M. H. Chen, and C. R. Wu (2013), Field observations of changes in SST, chlorophyll and POC flux in the Southern East China Sea before and after the passage of typhoon Jangmi, *Terr. Atmos. Ocean Sci.*, *24*(5), 899–910, doi:10.3319/TAO.2013.05.23.01(Oc).

Sun, L., Y. J. Yang, T. Xian, Z. M. Lu, and Y. F. Fu (2010), Strong enhancement of chlorophyll a concentration by a weak typhoon, *Mar. Ecol. Prog. Ser.*, *404*, 39–50, doi:10.3354/Meps08477.

Takahashi, T., J. Olafsson, J. G. Goddard, D. W. Chipman, and S. C. Sutherland (1993), Seasonal-variation of CO_2 and nutrients in the high-latitude surface oceans—A comparative-study, *Global Biogeochem. Cycles*, *7*(4), 843–878, doi:10.1029/93GB02263.

Takahashi, T., et al. (2002), Global sea-air CO_2 flux based on climatological surface ocean *p*CO2, and seasonal biological and temperature effects, *Deep Sea Res., Part II*, *49*(9–10), 1601–1622, doi:10.1016/s0967-0645(02)00003-6.

Tsuchiya, K., V. S. Kuwahara, T. Yoshiki, R. Nakajima, H. Miyaguchi, N. Kumekawa, T. Kikuchi, and T. Toda (2014), Phytoplankton community response and succession in relation to typhoon passages in the coastal waters of Japan, *J. Plankton Res.*, *36*(2), 424–438, doi:10.1093/plankt/fbt127.

Turk, D., C. J. Zappa, C. S. Meinen, J. R. Christian, D. T. Ho, A. G. Dickson, and W. R. McGillis (2010), Rain impacts on CO_2 exchange in the western equatorial Pacific Ocean, *Geophys. Res. Lett.*, *37*, L23610, doi:10.1029/2010GL045520.

Volk, T., and M. I. Hoffert (1985), Ocean carbon pumps: Analysis of relative strengths and efficiencies in ocean driven atmospheric CO_2 changes, in The Carbon Cycle and Atmospheric CO_2: Natural Variations Archean to Present, Geophys. Monogr. Ser., vol. 32, pp. 99–110, AGU, Washington, D. C.

Wada, A., T. Midorikawa, M. Ishii, and T. Motoi (2011), Carbon system changes in the East China Sea induced by typhoons Tina and Winnie in 1997, *J. Geophys. Res.*, *116*, C07014, doi:10.1029/2010JC006701.

Wang, G. H., J. L. Su, and P. C. Chu (2003), Mesoscale eddies in the South China Sea observed with altimeter data, *Geophys. Res. Lett.*, *30*(21), 2121, doi:10.1029/2003GL018532.

Wang, J. J., and D. L. Tang (2014), Phytoplankton patchiness during spring intermonsoon in western coast of South China Sea, *Deep Sea Res., Part II*, *101*, 120–128, doi:10.1016/j.dsr2.2013.09.020.

Wanninkhof, R. (1992), Relationship between wind-speed and gas-exchange over the ocean, *J. Geophys. Res.*, *97*(C5), 7373–7382, doi:10.1029/92JC00188.

Wanninkhof, R., A. Olsen, and J. Trinanes (2007), Air-sea CO_2 fluxes in the Caribbean Sea from 2002–2004, *J. Mar. Syst.*, *66*(1–4), 272–284, doi:10.1016/j.jmarsys.2006.11.014.

Weiss, R. F. (1974), Carbon dioxide in water and seawater: The solubility of a non-ideal gas, *Mar. Chem.*, *2*(3), 203–215, doi:10.1016/0304-4203(74)90015-2.

Ye, H. J., Y. Sui, D. L. Tang, and Y. Afanasyev (2013), A subsurface chlorophyll a bloom induced by typhoon in the South China Sea, *J. Mar. Syst.*, *128*, 138–145, doi:10.1016/j.jmarsys.2013.04.010.

Yu, J., D. L. Tang, Y. Z. Li, Z. R. Huang, and G. B. Chen (2013), Increase in fish abundance during two typhoons in the South China Sea, *Adv. Space Res.*, *51*(9), 1734–1749, doi:10.1016/j.asr.2012.11.019.

Yu, J., D. L. Tang, G. B. Chen, Y. Z. Li, Z. R. Huang, and S. F. Wang (2014), The positive effects of typhoons on the fish CPUE in the South China Sea, *Cont. Shelf Res.*, *84*, 1–12, doi:10.1016/j.csr.2014.04.025.

Zhai, W. D., M. H. Dai, W. J. Cai, Y. C. Wang, and Z. H. Wang (2005), High partial pressure of CO_2 and its maintaining mechanism in a subtropical estuary: The Pearl River estuary, China, *Mar. Chem.*, *93*(1), 21–32, doi:10.1016/j.marchem.2004.07.003.

Zhai, W. D., M. Dai, and W. J. Cai (2009), Coupling of surface pCO_2 and dissolved oxygen in the northern South China Sea: Impacts of contrasting coastal processes, *Biogeosciences*, *6*(11), 2589–2598, doi:10.5194/bg-6-2589-2009.

Zhai, W. D., M. H. Dai, B. S. Chen, X. H. Guo, Q. Li, S. L. Shang, C. Y. Zhang, W. J. Cai, and D. X. Wang (2013), Seasonal variations of sea-air CO_2 fluxes in the largest tropical marginal sea (South China Sea) based on multiple-year underway measurements, *Biogeosciences*, *10*(11), 7775–7791, doi:10.5194/bg-10-7775-2013.

Zhao, H., D. L. Tang, and Y. Q. Wang (2008), Comparison of phytoplankton blooms triggered by two typhoons with different intensities and translation speeds in the South China Sea, *Mar. Ecol. Prog. Ser.*, *365*, 57–65, doi:10.3354/Meps0741838.

Zhao, H., D. L. Tang, and D. X. Wang (2009), Phytoplankton blooms near the Pearl River Estuary induced by Typhoon Nuri, *J. Geophys. Res.*, *114*, C12027, doi:10.1029/2009JC005384.

Zheng, Z.-W., C.-R. Ho, and N.-J. Kuo (2008), Importance of pre-existing oceanic conditions to upper ocean response induced by Super Typhoon Hai-Tang, *Geophys. Res. Lett.*, *35*, L20603, doi:10.1029/2008GL035524.

Zhou, K. B., M. H. Dai, S.-J. Kao, L. Wang, P. Xiu, F. Chai, J. W. Tian, and Y. Liu (2013), Apparent enhancement of 234Th-based particle export associated with anticyclonic eddies, *Earth Planet. Sci. Lett.*, *381*, 198–209, doi:10.1016/j.epsl.2013.07.039.